

**PAPER****Direct generation of genuine single-longitudinal-mode narrowband photon pairs****OPEN ACCESS****RECEIVED**

19 March 2015

REVISED

18 June 2015

ACCEPTED FOR PUBLICATION

18 June 2015

PUBLISHED

3 August 2015

Content from this work
may be used under the
terms of the [Creative
Commons Attribution 3.0
licence](#).

Any further distribution of
this work must maintain
attribution to the
author(s) and the title of
the work, journal citation
and DOI.

**Kai-Hong Luo, Harald Herrmann, Stephan Krapick, Benjamin Brecht, Raimund Ricken, Viktor Quiring, Hubertus Suche, Wolfgang Sohler and Christine Silberhorn**

Integrated Quantum Optics, Applied Physics, University of Paderborn, Warburger Str. 100, 33098, Paderborn, Germany

E-mail: khluo@mail.uni-paderborn.de**Keywords:** integrated quantum optics, narrowband photon source, nonlinear waveguidesSupplementary material for this article is available [online](#)**Abstract**

The practical prospect of quantum communication and information processing relies on sophisticated single-photon pairs, which feature a controllable waveform, narrow spectrum, excellent purity, fiber compatibility, and miniaturized design. For practical realizations, stable, miniaturized, low-cost devices are required. Sources with one or some of the above characteristics have already been demonstrated, but it is quite challenging to obtain a source with all of the described characteristics simultaneously. Here we report on an integrated single-longitudinal-mode, non-degenerate, narrowband photon pair source that exhibits all the requirements needed for quantum applications. The device is composed of a periodically poled, Ti-indiffused, lithium niobate waveguide with high reflective dielectric mirror coatings deposited on the waveguide end-faces. Photon pairs with wavelengths around 890 and 1320 nm are generated via type II phase-matched parametric down-conversion (PDC). Clustering in this dispersive cavity restricts the whole conversion spectrum to one single-longitudinal mode in a single cluster, yielding a narrow bandwidth of only 60 MHz. The high conversion efficiency in the waveguide, together with the spectral clustering in the doubly resonant waveguide, leads to a high brightness of 3×10^4 pairs/(s mW MHz). This source exhibits prominent single-longitudinal-mode purity and remarkable temporal shaping capability. In particular, due to temporal broadening, we can observe that the coherence time of the two-photon component of the PDC state is actually longer than that of the single-photon states. The miniaturized monolithic design enables this source to have various fiber communication applications.

1. Introduction

Quantum communication and information processing (QCIP) [1, 2] currently is evolving from fundamental research towards real-life applications. This process can be strongly fostered by the implementation of integrated optical devices offering miniaturized and potentially low-cost components for applications in quantum key distribution [1], long-distance quantum communication [3], quantum repeaters [4], and quantum networks [5]. Moreover, compact and rugged integrated optical quantum circuits [6–10] with high functionality can efficiently replace bulky implementations to pave the way to practical applications.

In particular, quantum repeater architectures have been proposed [4, 11, 12] to overcome the current limitations of long-distance quantum communication due to transmission losses. These typically require spectrally narrowband two-color photon pairs, for instance, to address the absorption line of the storage medium in a quantum memory (QM) [13–18] with one photon and transmit the second over a fiber network. Such QMs usually have their absorption in the visible or near infrared, i.e., far away from the telecommunication range. The corresponding bandwidths are typically in the range of MHz to GHz, depending on different storage regimes (like spin-wave storage in cold atomic ensembles and atomic-frequency-comb echoes in solid state and room-temperature storage). Among the most promising materials for high-bandwidth QMs are solid-state

Table 1. Recent results of cavity-enhanced PDC are shown in the table. All sources except ours, described in the last column, used bulk crystals to generate narrowband photon pairs, which either feature single-mode operation, have high brightness, or combine a fiber network with quantum memory. For comparison, the last column shows the results of the integrated source reported in this paper.

PDC	Bao <i>et al</i> [30]	Scholz <i>et al</i> [31]	Chuu <i>et al</i> [39]	Fekete <i>et al</i> [41]	This paper
Wavelength (nm)	780	893	1064	606 + 1436	890 + 1320
Bandwidth (MHz)	9.6	2.7	8.3	1.7	60
Brightness ($\frac{\text{pairs}}{\text{s mW MHz}}$)	6	330	1.34×10^4	11	3×10^4
Mode selectivity	multi-mode	single-mode	—	few modes	single-mode
Fiber compatibility	—	—	✓	✓	✓
Atom interaction	Rb (MHz)	Cs (MHz)	—	Pr (MHz)	Nd (100 MHz)
Cavity locking	single cavity	double cavity	no	double cavity	no

atomic ensembles, specifically rare-Earth ion-doped crystals or glasses [19–22] and QM at room temperature [23, 24].

A widespread method to generate photon pairs is parametric down conversion (PDC) [25]. In such a PDC process, a medium with $\chi^{(2)}$ nonlinearity splits a single pump photon into two photons of lower energy, named signal and idler, obeying energy conservation and phase matching. However, the loose phase-matching condition for both bulk and waveguide sources usually leads to a continuous broad bandwidth, typically exceeding several 100 GHz and a mixed state in frequency. To overcome this bottleneck, narrowband photon-pair sources are desired with an adapted bandwidth and a high spectral brightness.

One promising approach to generate such narrowband photon pairs is to use resonance enhancement of PDC within a cavity, also called an optical parametric oscillator (OPO), far below the threshold [27–44]. PDC is enhanced at the resonances of the cavity but inhibited at non-resonant frequencies. An overview over the most important resonant PDC sources published so far is given in table 1. Despite enormous progress—non-degenerate photon pairs with linewidths of about 2 MHz oscillating on four longitudinal modes—which was obtained in the bulk cavity [41], most of the bulk sources suffer from low pair-production efficiency, degenerate frequency, bad mode selectivity, and complicated cavity-locking techniques.

To overcome these limitations, strong benefits from a monolithic implementation of this scheme can be expected. Recently a high-Q cavity using a whispering gallery mode resonator has been demonstrated to achieve single-mode photon pairs [42]. An alternative approach using a periodically poled lithium niobate (PPLN) waveguide with dielectric mirrors deposited on its end-faces has been demonstrated to generate nearly degenerate photon-pairs via a type I phase-matched PDC process in the telecom region [36]. However, it exhibited a limited mode selectivity, because the spectrum consisted of a series of longitudinal modes due to the small difference of the free spectral ranges (FSRs) of signal and idler close to degeneracy. A detailed theoretical study [37] indicates that exploiting type II phase matching should strongly limit the number of longitudinal modes, because the large birefringence provides a larger difference of the FSRs and thus fosters the spectral narrowing.

The drawback of the resonant sources reported so far is that they either achieve narrow bandwidth, operate single-mode, reach high brightness, or combine two wavelengths for atomic transition and fiber communications. However, for practical quantum application, sources which provide simultaneously all the above-mentioned properties are required. In this paper, we present the experimental realization of such a miniaturized, two-color, integrated, bright narrowband photon pair source based on a doubly resonant waveguide exploiting type II phase matching, exhibiting one longitudinal mode.

In section 2 we will discuss in detail the principle of operation and the underlying physical theory. In the non-degenerate case, birefringence and material dispersion result in different FSRs for signal and idler. As maximum efficiency is only obtained if both signal and idler are resonant simultaneously, PDC is generated only in certain regions of the spectrum, the so-called ‘clusters’ [45, 46]. In this way the spectral density is redistributed in comparison to the non-resonant case, and, thus, ideally a completely filter-free source with actively reduced bandwidth can be realized without sacrificing any photon flux level. In sections 3 and 4, details on the waveguide fabrication and the experimental set-up are given, respectively. The practical implementation is challenging, because it requires loss minimization, short poling periods for phase-matching, and, specifically, tailored mirror coatings for both signal and idler photons. In section 5 the experimental results are discussed and compared with the theoretically predicted ones. Our engineered clustering in the dispersive cavity restricts the conversion to a single longitudinal mode operation with a spectral linewidth around 60 MHz and high spectral brightness 3×10^4 pairs/(s mW MHz). Such a non-degenerate PDC photon pair source can be applied in a quantum repeater, addressing a Nd-based QM with one photon and combining the other with a fiber network.

2. Principle and theory

2.1. Nonresonant PDC process

PDC is an important process in quantum optics, used especially as a source of entangled photon pairs and of single photons. In a nonlinear $\chi^{(2)}$ medium pump, photons (at frequency ω_p) are split into pairs of photons (signal ω_s and idler ω_i , respectively), obeying energy and momentum conservation. As for most cases the latter cannot be obtained in homogeneous crystals, quasi-phase matching is exploited in a periodically inverted medium. Thus, the phase-matching condition becomes:

$$\Delta k = k(\omega_p) - k(\omega_s) - k(\omega_i) - \frac{2\pi}{\Lambda} \approx 0 \quad (1)$$

where k_j ($j = p, s, i$) are the propagation constants of the pump, signal, and idler fields, and Λ is the poling period. We express the state of the photon pairs generated by PDC up to the second-order expansion,

$$\begin{aligned} |\Psi\rangle_{\text{PDC}} \propto & \int d\omega_s d\omega_i f(\omega_s, \omega_i) \hat{a}_s^\dagger(\omega_s) \hat{a}_i^\dagger(\omega_i) |0\rangle \\ & + \int d\omega_s d\omega'_s d\omega_i d\omega'_i f(\omega_s, \omega_i) f(\omega'_s, \omega'_i) \hat{a}_s^\dagger(\omega_s) \hat{a}_s^\dagger(\omega'_s) \hat{a}_i^\dagger(\omega_i) \hat{a}_i^\dagger(\omega'_i) |0\rangle, \end{aligned} \quad (2)$$

where $\hat{a}_{s,i}^\dagger(\omega_{s,i})$ describes the photon creation operator at frequency $\omega_{s,i}$, and $f(\omega_s, \omega_i)$ is the joint spectral function (JSF) of the nonlinear waveguide:

$$f(\omega_s, \omega_i) = \alpha(\omega_s + \omega_i) \times \varphi(\omega_s, \omega_i). \quad (3)$$

The $\alpha(\omega_s + \omega_i)$ describes the spectrum and the amplitude of the pump field, $\varphi(\omega_s, \omega_i)$ is a phase-matching function $\text{sinc}[\Delta k(\omega_s, \omega_i) \frac{L}{2}] \exp[i\Delta k(\omega_s, \omega_i) \frac{L}{2}]$.

The full-width at half-maximum (FWHM) of the PDC process in the waveguide is determined by the phase-matching condition. Assuming a monochromatic pump, i.e., $\alpha(\omega_s + \omega_i) \propto \delta(\omega_s + \omega_i)$, Δk can be linearized

$$\Delta k(\omega_{s,i}) \approx \Delta k_0 + \frac{1}{c} [n_{gs} - n_{gi}] \Delta \omega_{s,i}, \quad (4)$$

where n_{gs} and n_{gi} are the group index of signal and idler, respectively. The spectral characteristics of the PDC process are given by a $\text{sinc}^2[\Delta k(\omega_s, \omega_i) \frac{L}{2}]$ function. Thus, the FWHM of the signal photons generated in a waveguide of length L is given by:

$$\Delta \nu_s^{\text{FWHM}} \approx 5.56 \frac{c}{2\pi L} \frac{1}{|n_{gs} - n_{gi}|}; \quad (5)$$

i.e., the spectral bandwidth is inversely proportional to the difference of the group velocities of signal and idler. Thus, close to degeneracy the bandwidth is very large, whereas group velocity dispersion in most cases leads to a much narrower bandwidth far away from degeneracy.

2.2. Resonant PDC

Our source exploits photon pair generation by PDC within a cavity. The schematic of the integrated source is shown in figure 1(a). The resonant waveguide is a Fabry-Pérot cavity with asymmetric reflectivities ($R_{1s,i}$ and $R_{2s,i}$), internal loss ($\alpha_{s,i}$), and effective indices $n(\omega_{s,i})$ for the fundamental modes at signal and idler wavelength, respectively. The photon-pair state generated within such a resonator can be expressed by:

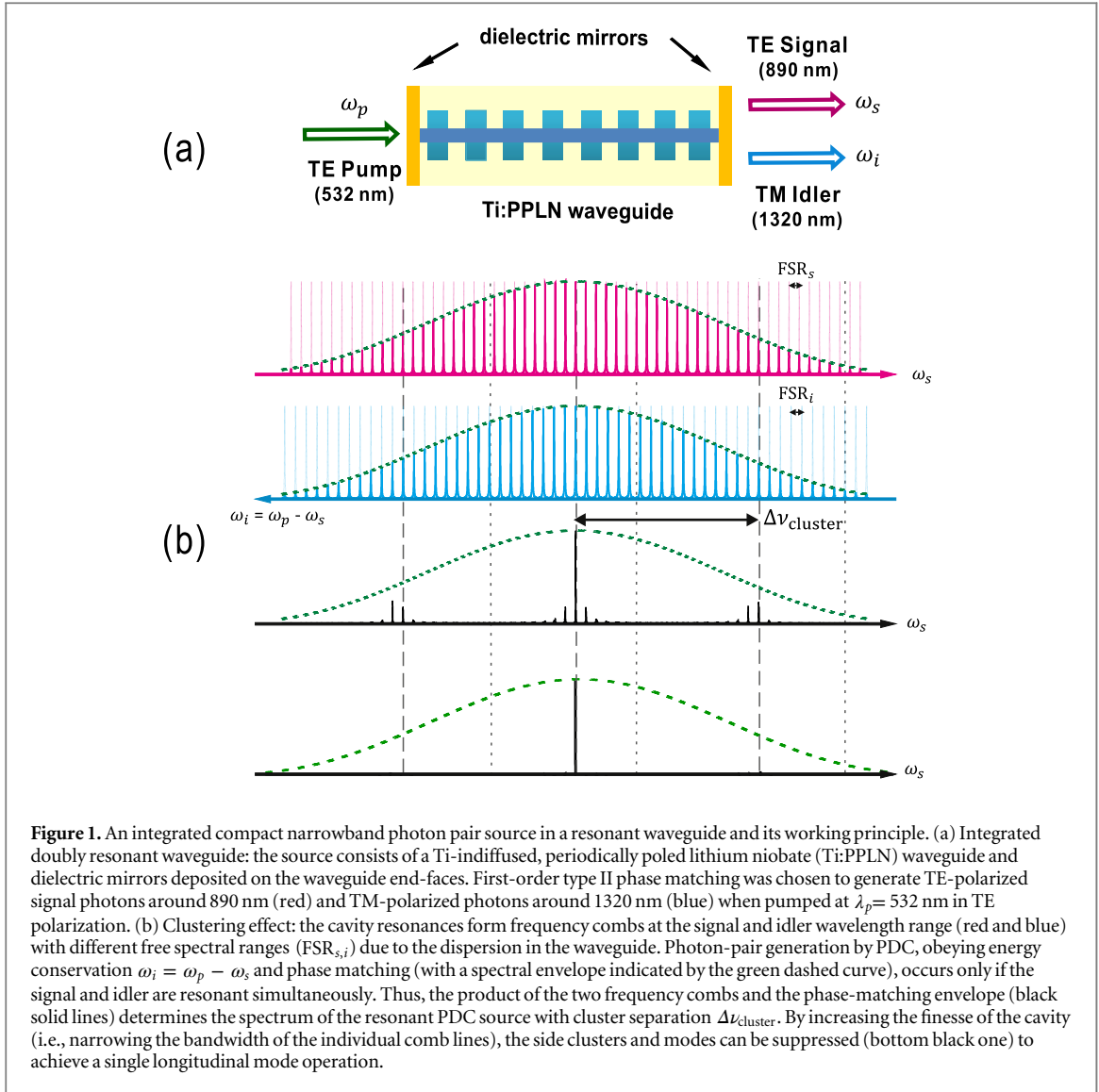
$$\begin{aligned} |\Psi\rangle_{\text{RPDC}} \propto & \int d\omega_s d\omega_i f_R(\omega_s, \omega_i) \hat{a}_s^\dagger(\omega_s) \hat{a}_i^\dagger(\omega_i) |0\rangle \\ & + \int d\omega_s d\omega'_s d\omega_i d\omega'_i f_R(\omega_s, \omega_i) f_R(\omega'_s, \omega'_i) \hat{a}_s^\dagger(\omega_s) \hat{a}_s^\dagger(\omega'_s) \hat{a}_i^\dagger(\omega_i) \hat{a}_i^\dagger(\omega'_i) |0\rangle, \end{aligned} \quad (6)$$

where $f_R(\omega_s, \omega_i)$ is the cavity-modified JSF: $f_R(\omega_s, \omega_i) = f(\omega_s, \omega_i) A_s(\omega_s) A_i(\omega_i)$, with $f(\omega_s, \omega_i)$ being the conventional JSF for the nonresonant PDC. $A_{s,i}(\omega_{s,i})$ are proportional to the field distributions inside the cavity. They can easily be derived, treating the device as a classical Fabry-Pérot resonator with internal loss:

$$A_{s,i}(\omega_{s,i}) = \frac{\sqrt{(1 - R_{1s,i})(1 - R_{2s,i})} e^{-\alpha_{s,i}L/2}}{1 - \sqrt{R_{1s,i}R_{2s,i}} e^{-\alpha_{s,i}L} e^{i2\omega_{s,i}n(\omega_{s,i})L/c}}. \quad (7)$$

Therefore, we obtain an expression for the resulting joint spectral intensity,

$$S_R(\omega_s, \omega_i) = |f_R(\omega_s, \omega_i)|^2 = |f(\omega_s, \omega_i)|^2 \mathcal{A}_s(\omega_s) \mathcal{A}_i(\omega_i), \quad (8)$$



where $\mathcal{A}_{s,i}(\omega_{s,i}) = |A_{s,i}(\omega_{s,i})|^2$ are Airy functions of signal and idler photons, respectively. The bandwidth of each cavity mode is related to the finesse; more details in appendix A. Therefore the spectral characteristics are a product of the phase-matching sinc function and two combs of Lorentzian lines, spaced by the resonator's FSRs.

The explicit form of the signal spectrum can be determined completely as

$$S_R(\omega_s) \propto \left| \int d\omega_i f_R(\omega_s, \omega_i) \right|^2 \propto \text{sinc}^2 \left[\Delta k(\omega_s) \frac{L}{2} \right] \mathcal{A}_s(\omega_s) \mathcal{A}_i(\omega_p - \omega_s). \quad (9)$$

2.3. Cluster effect

In the dispersive waveguide, cavity resonances occur at distinct frequencies separated by the FSR of the resonator. These resonances form frequency combs spaced with respective FSRs in the signal and idler wavelength range (as shown in the supplementary movie).

$$FSR_{s,i} \approx \frac{c}{2n_{gs,i}L} \quad (10)$$

The FSR is the inverse of the round-trip time of a photon in the cavity.

The FWHM of each resonance $\Delta\nu$ is related with the finesse \mathcal{F} of the cavity:

$$\mathcal{F}_{s,i} = \frac{\text{FSR}_{s,i}}{\Delta\nu_{s,i}} = \frac{\pi\sqrt{\sqrt{R_{1,s,i}}R_{2,s,i}}e^{-\alpha_{s,i}L}}{\left(1 - \sqrt{R_{1,s,i}}R_{2,s,i}\right)e^{-\alpha_{s,i}L}}. \quad (11)$$

For the type I degenerate case, the frequency combs of signal and idler photons are identical. Thus, PDC generation still happens at all comb frequencies within the phase-matching bandwidth. However, for type II and/or a degenerate case, there are different FSRs in the resonant waveguide due to the different group dispersions at the signal and idler wavelengths, as shown in the upper two curves in figure 1(b). Thus, corresponding resonances of signal and idler only overlap at a certain frequency, but adjacent modes do not coincide, as shown in the bottom curve in figure 1(b). For instance, if a pair is simultaneously resonant for, e.g., ω_{s0} and ω_{i0} , the adjacent signal resonance lies at $\omega_{s0} + 2\pi\text{FSR}_s$, and the corresponding idler frequency at $\omega_{i0} - 2\pi\text{FSR}_i$ is not in the resonance peak due to the different FSRs. The couple of simultaneous resonances for signal and idler is called a cluster [37, 45]. However, after a certain number of FSRs, another cluster occurs again, if the phase-matching bandwidth is broad enough. This happens when N_0 (where N_0 is the number of FSRs in one cluster) times the signal FSR equals $N_0 - 1$ times the idler FSR. Thus, the cluster separation $\Delta\nu_{\text{cluster}}$, i.e., the frequency spacing between clusters, is given by:

$$\Delta\nu_{\text{cluster}} = N_0 \cdot \text{FSR}_s = \frac{1}{|n_{gi} - n_{gs}|} \frac{c}{2L}, \quad (12)$$

which is associated with the difference of the group indices. By comparing equations (5) and (12), we can see that the cluster separation $\Delta\nu_{\text{cluster}}$ is slightly larger than half of the bandwidth of the PDC phase-matching envelope $\Delta\nu_s^{\text{FWHM}}$. Therefore, the maximum number of clusters within the phase-matching range is three. Theoretically, if there is a dominant cluster in the center of the normalized phase-matching curve, two symmetric clusters will occur at the side wings of the envelope with about 41% weight. However, the fine-mode structures inside clusters are determined by signal and idler resonances. As shown in figure 1(b), the intensity of PDC emission in the two side clusters is weaker than the central cluster. Within a single cluster, the number of resonances contributing to the PDC generation depends on the bandwidth of the resonances and the difference of the FSRs.

Due to the spectral density redistribution in the cavity, PDC in the resonant waveguide is enhanced due to cavity narrowing and the cluster effect. The enhancement factor M is given by

$$M = \frac{\int d\omega_s \int d\omega_i |f(\omega_s, \omega_i)|^2}{\int d\omega_s \int d\omega_i |f(\omega_s, \omega_i)|^2 \mathcal{A}_s(\omega_s) \mathcal{A}_i(\omega_i)} \sim \eta_{\text{pp}} \mathcal{F}_s \mathcal{F}_i N_0, \quad (13)$$

where η_{pp} is the photon pair escape probability defined by the ratio of the number of photon pairs, which leaves the cavity to the number of pairs created inside the cavity. More details are discussed in appendix B. Equation (13) tells us that the higher the finesse of the cavity is, the more enhancement can be achieved [27]. The enhancement factor is roughly proportional to the square of the finesse of the cavity.

However, for a waveguide-based resonant PDC source, the internal losses must be considered. (In bulk-type sources, these might be neglected due to the much smaller losses in bulk crystals compared to waveguides.) The higher the finesse is, the larger the number of round-trips is. Thus, the probability that a created photon pair is lost within the cavity increases with increasing the finesse. Hence, η_{pp} decreases with increasing the finesse by higher mirror reflectivities, keeping waveguide length and losses constant. On the other hand, the spectral redistribution due to the clustering results in a N_0 times increased spectral density at the synchronous signal and idler resonance.

2.4. Two-photon cross-correlation function

To verify the photon pairs generation and to evaluate its efficiency, the standard way is to measure the cross-correlation between two generated photons. The two-photon cross-correlation function $G_{si}^{(1,1)}$ between signal and idler photons defines the shape of the coincidence events. Each resonance of the frequency comb of signal and idler can reasonably well be approximated by a Lorentzian function $A_{s,i}(\omega_{s,i}) \propto (\gamma_{s,i} + i\omega_{s,i})^{-1}$, where $\gamma_{s,i}$ describes the damping constants of the cavity. Assuming only a single pair of signal ω_s and idler modes ω_i are synchronously resonant with narrowband range $\delta\omega$, we get the complex JSF

$$f_R(\delta\omega) = \frac{\gamma_s}{\gamma_s + i\delta\omega} \frac{\gamma_i}{\gamma_i - i\delta\omega}. \quad (14)$$

The temporal $G_{si}^{(1,1)}(\tau)$ is measured as the coincidence distribution of detection time differences $\tau = t_s - t_i$ between the signal and idler photons,

$$G_{si}^{(1,1)}(\tau) = \left\langle \hat{a}_s^\dagger(t) \hat{a}_i^\dagger(t+\tau) \hat{a}_i(t+\tau) \hat{a}_s(t) \right\rangle = \left| \tilde{f}_R(\tau) \right|^2, \quad (15)$$

where $\tilde{f}_R(\tau)$ is the joint temporal function (JTF) defined as the inverse Fourier transform of the JSF. Thus, the signal-idler correlation can be simplified as

$$G_{si}^{(1,1)}(\tau) \propto u(\tau) e^{-2\gamma_s \tau} + u(-\tau) e^{2\gamma_i \tau}, \quad (16)$$

where $u(\tau)$ is the step function. This shows that the coincidence function is determined by two different exponentially decaying functions, which are related to the damping of signal and idler photons, respectively. Thus, in most cases $G_{si}^{(1,1)}(\tau)$ is asymmetric due to $\gamma_s \neq \gamma_i$. The signal-idler correlation time is defined by $\tau_c \sim 2(\tau_s + \tau_i)/e$. This means we can identify the lifetime of signal/idler $\tau_{s,i} = (2\gamma_{s,i})^{-1}$ from the signal-idler coincidence measurements. Only if $\tau_s = \tau_i$, which, for instance, is always the case if type I degenerate PDC processes are exploited [36], one gets a symmetric cross-correlation with correlation time $\tau_c \sim 4\tau_s/e$.

2.5. Two-photon auto-correlation function

Besides the one-photon pairs generated in the PDC process, it is still possible to generate double or higher photon pairs, as shown in equation (6). The temporal second-order auto-correlation function $G^{(2)}(\tau)$ of signal and idler photons, respectively, is related to the temporal coherence of the two-photon wave-packet component. The measurement of the auto-correlation is usually performed by inserting a 50:50 beam splitter into the signal (idler) arm and detecting the photons at the two output ports of the beam splitter with single-photon detectors. If coincidence clicks are registered, a second- (or higher) order photon pair generation must have happened. $G^{(2)}(\tau)$ is defined by

$$\begin{aligned} G^{(2)}(\tau) &= \left\langle \hat{a}^\dagger(t) \hat{a}^\dagger(t+\tau) \hat{a}(t+\tau) \hat{a}(t) \right\rangle \\ &= \left\langle \hat{a}^\dagger(t) \hat{a}(t) \right\rangle \left\langle \hat{a}^\dagger(t+\tau) \hat{a}(t+\tau) \right\rangle \\ &\quad + \left\langle \hat{a}^\dagger(t) \hat{a}(t+\tau) \right\rangle \left\langle \hat{a}^\dagger(t+\tau) \hat{a}(t) \right\rangle. \end{aligned} \quad (17)$$

Thus, the normalized second-order auto-correlation function $g^{(2)}(\tau)$ is given by

$$g^{(2)}(\tau) = 1 + \left| \frac{\left\langle \hat{a}^\dagger(t) \hat{a}(t+\tau) \right\rangle}{\left\langle \hat{a}^\dagger(t) \hat{a}(t) \right\rangle} \right|^2 = 1 + \left| g^{(1)}(\tau) \right|^2. \quad (18)$$

Consider a signal-cavity mode with a Lorentzian spectral distribution,

$$f_s(\delta\omega) = \frac{\gamma_s}{\gamma_s + i\delta\omega} \frac{\gamma_i}{\gamma_i - i\delta\omega}; \quad (19)$$

the time-dependent correlation function is given by the inverse Fourier transform of its intensity spectrum,

$$\begin{aligned} &\left\langle \hat{a}^\dagger(t) \hat{a}(t+\tau) \right\rangle \\ &= \mathcal{FT}^{-1} [f_s(\delta\omega) f_s^*(\delta\omega)] = \frac{1}{4} \gamma_s \gamma_i e^{-\gamma_s |\tau|} * e^{-\gamma_i |\tau|} \\ &= \begin{cases} \frac{\gamma_s \gamma_i}{\gamma_i^2 - \gamma_s^2} \left[\frac{1}{2} \gamma_s e^{-\gamma_s |\tau|} - \frac{1}{2} \gamma_i e^{-\gamma_i |\tau|} \right], & \gamma_s \neq \gamma_i \\ \frac{1}{4} \gamma_s (1 + \gamma_s |\tau|) e^{-\gamma_s |\tau|}, & \gamma_s = \gamma_i \end{cases}. \end{aligned} \quad (20)$$

Correspondingly, equation (18) can be deduced as

$$\begin{aligned} g^{(2)}(\tau) &= 1 + \left| g_0^{(1)}(\tau) \right|^2 \\ &= \begin{cases} 1 + \left| \frac{1}{\gamma_i - \gamma_s} e^{-\frac{\gamma_s + \gamma_i}{2} |\tau|} \left(\gamma_i e^{\frac{\gamma_i - \gamma_s}{2} |\tau|} - \gamma_s e^{-\frac{\gamma_i - \gamma_s}{2} |\tau|} \right) \right|^2, & \gamma_s \neq \gamma_i \\ 1 + \left| e^{-\gamma_s |\tau|} (1 + \gamma_s |\tau|) \right|^2, & \gamma_s = \gamma_i \end{cases}. \end{aligned} \quad (21)$$

The above equation shows that the decay of the auto-correlation is not an exponential decay anymore. For our further analysis, it is useful to estimate the shape and half-width of the auto-correlation peak. By using a Taylor expansion, the above complicated function can be approximately simplified to

$$\begin{aligned}
g^{(2)}(\tau) &\simeq 1 + \left| e^{-\frac{1}{2}(\gamma_s + \gamma_i)|\tau|} \left(1 + \frac{1}{2}(\gamma_s + \gamma_i)|\tau| \right) \right|^2 \\
&\approx 1 + \left(1 + \left[\frac{1}{2}(\gamma_s + \gamma_i)\tau \right]^2 \right)^{-1}.
\end{aligned} \tag{22}$$

From equation (22), we can conclude that the auto-correlation peak is symmetric, no matter which kind of PDC process it produced. This shows an intrinsic difference to the behavior of the cross-correlation function with its asymmetrically exponential decays. The decay of auto-correlation can be approximated as a Cauchy-Lorentz distribution. We can define the auto-correlation time T_{au} as the FWHM of the auto-correlation function and obtain

$$T_{au} \approx \frac{4}{\gamma_s + \gamma_i} \approx \frac{2}{\ln 2} \tau_c. \tag{23}$$

We find that the auto-correlation time exceeds the cross-correlation time by a factor of around 2.8. Our theoretical analysis is in good agreement with previous experimental observations [32, 40].

Another way of interpreting this auto-correlation is to consider the measurement from the multiple-photon pair-generation point of view. If two single-photon detectors in the signal (or idler) arm register a coincidence click, the second- (or higher) order part of the PDC state (second term in equation (6)) is probed. In contrast, the cross-correlation measurement provides mainly information about the first-order part. The auto-correlation time T_{au} is the correlation time between the two-photon components of signal (or idler) photon components, while the cross-correlation time τ_c is the correlation time between signal and idler photons. In the temporal domain, the auto-correlation time T_{au} is larger than correlation time τ_c . Correspondingly, two photon components have narrower frequency bandwidth (related to $f(\omega_s, \omega_i)f(\omega'_s, \omega'_i)$) than the one-photon pair component (related to $f(\omega_s, \omega_i)$).

2.6. Heralded correlation function

To confirm the nonclassical property of generated narrowband photons, it is important to characterize heralded photons. The conditional auto-correlation function is defined by [48]

$$g_{\text{heralded}}^{(2)}(t_{s1}, t_{s2} | t_i) = \frac{P_{ssi}(t_{s1}, t_{s2}, t_i)}{R^3 g_{si}^{(1,1)}(t_{s1} - t_i) g_{si}^{(1,1)}(t_{s2} - t_i)}, \tag{24}$$

where $P_{ssi}(t_{s1}, t_{s2}, t_i)$ is the triple coincidence rate and R is the pair-generation rate. After simplification, the function of interest, $g_{\text{heralded}}^{(2)}(\tau) = g_{\text{heralded}}^{(2)}(t_i, t_i + \tau | t_i)$, can be represented as

$$g_{\text{heralded}}^{(2)}(\tau) \approx 1 - \exp \left[-2 \left(\frac{\gamma_s \gamma_i}{\gamma_s + \gamma_i} \tau \right)^2 \right], \tag{25}$$

which means the heralded correlation can be approximated by a Gaussian distribution. T_{he} is the heralded time between one (signal or idler) photon component,

$$T_{he} \approx \frac{2}{\gamma_s + \gamma_i} = \frac{1}{2} T_{au}. \tag{26}$$

3. Waveguide resonator fabrication

To study experimentally such a resonant PDC source, a PPLN waveguide with dielectric coatings at its end faces was fabricated. It was designed to provide type II phase matching for a PDC process with a TE-polarized pump at 532 nm for the generation of photon pairs at 890 nm (TE-polarized) and 1320nm (TM-polarized).

3.1. Ti:PPLN waveguide

The waveguide was fabricated by an indiffusion of a lithographically patterned, 81 nm-thick, 5 μm -wide Ti-stripe into the Z-cut LiNbO₃ substrate. The diffusion parameters were designed to provide single-mode guiding at the TM-polarized idler mode. At signal and pump wavelength, however, the waveguide supports several guided modes.

Subsequent to the Ti-indiffusion, the periodic poling was performed. To obtain first-order phase matching for the selected wavelength combination, a short poling period of only $\Lambda \approx 4.44 \mu\text{m}$ is required. This could be achieved using a field-assisted domain inversion of the lithographically defined poling pattern. In the final

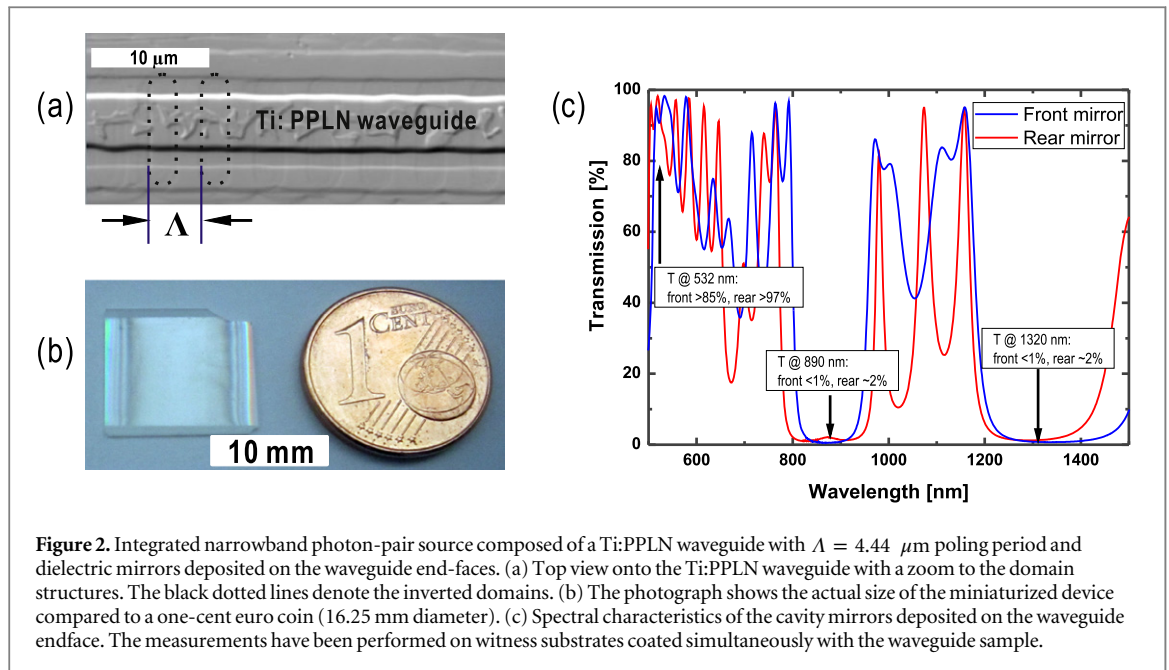


Figure 2. Integrated narrowband photon-pair source composed of a Ti:PPLN waveguide with $\Lambda = 4.44 \mu\text{m}$ poling period and dielectric mirrors deposited on the waveguide end-faces. (a) Top view onto the Ti:PPLN waveguide with a zoom to the domain structures. The black dotted lines denote the inverted domains. (b) The photograph shows the actual size of the miniaturized device compared to a one-cent euro coin (16.25 mm diameter). (c) Spectral characteristics of the cavity mirrors deposited on the waveguide endface. The measurements have been performed on witness substrates coated simultaneously with the waveguide sample.

fabrication process the end faces were polished. Special care was taken to ensure flatness and parallelism of the waveguide end faces to avoid excess loss of the resonating waves at the multiple reflections at these interfaces.

3.2. Resonator

Based on the theoretical design rules discussed in the previous section and appendix A, the resonator finesse should exceed 20 to provide the spectral narrowing. The detailed structure of the integrated waveguide chip and experimental setup to study this resonant source are shown in figure 2. The source consists of a 12.3 mm-long Ti-indiffused waveguide in Z-cut PPLN and dielectric mirrors deposited on the waveguide end faces.

To implement the resonant source, dielectric layers composed of alternating layers of SiO_2 and TiO_2 were deposited on the end faces of the waveguide. In practice, a stack with 17 layers deposited as a front mirror provides a reflectivity of $R_{s,i} \approx 99\%$ for signal and idler wavelengths, and the rear mirror, consisting of 17 layers has the targeted $R_{s,i} \approx 98\%$ for both. The reflectivities of front and rear mirrors at 532 nm are around 15% and 13%, respectively, to enable efficient incoupling of the pump and to prevent triple resonance effects.

After mirror deposition, the resonator was characterized by measuring signal and idler decay times. As we discuss in appendix B, we obtained a finesse of $\mathcal{F} \sim 100$ and $\mathcal{F} \sim 80$ for the signal and idler wavelengths, respectively.

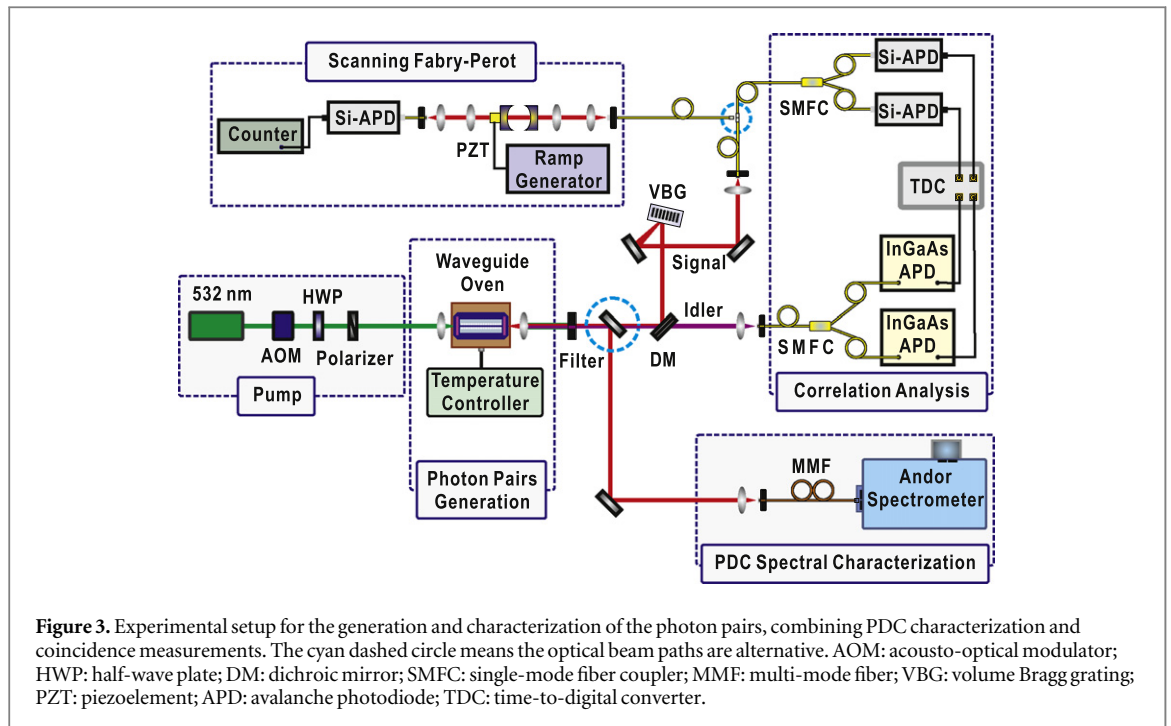
With the asymmetry of the mirror reflectivities, the ratio of outcoupled signal (idler) photons to lost photons before escaping this cavity is about $\eta_s \approx 0.28$ ($\eta_i \approx 0.18$), respectively. Thus, the overall photon-pair escape probability is given as $\eta_{\text{pp}} = \eta_s \eta_i$, which means about 5% of the generated photon pairs leave the cavity as couples at the desired output mirror. Therefore, the cavity-enhanced source provides high heralding efficiency.

The spatial profiles of signal and idler are determined by the waveguide properties. Both are the fundamental modes of the waveguide. Thus, the profiles are well matched for fiber network applications.

4. Experimental setup

The experimental setup to study this resonant source is shown in figure 3. The sample is pumped with a laser at 532 nm with a specified bandwidth of less than 1 MHz. To mitigate photorefraction, pump pulses with a typical length of about 200 ns and a repetition rate of about 100 kHz are extracted from the cw-source by using an acousto-optical modulator (AOM). A half-wave plate (HWP) together with a polarizer enable pump peak power tuning from 0.1–10 mW. The sample is heated to temperatures around 160 °C to obtain quasi-phase matching for the desired wavelength combination and to prevent luminescence and deterioration due to photorefraction. During the measurements the sample temperature is stabilized to about ± 1 mK. Coarse wavelength tuning can be accomplished by changing the poling period, while fine tuning of the resonance frequency is accomplished by varying the optical path length in the waveguide, for instance, by temperature tuning.

To characterize the generated PDC spectrum, the signal output from the waveguide is coupled to a spectrometer system (Andor Shamrock 303i with iKon-M 934 CCD camera) with a resolution of about 0.15 nm.



This measurement method provides a coarse overview over the spectral structure, but the resolution is still not sufficient to study details of the spectra within a single cluster. Thus, a volume Bragg grating (VBG, OptiGrate 900) with a spectral bandwidth of 0.17 nm is inserted into the signal beam path, as shown in figure 3, to act as a bandpass filter to select a single cluster. The filtered light is routed via a single-mode fiber to a scanning confocal Fabry–Pérot resonator with 15 GHz FSR and a finesse of about 20. Its transmission is analyzed using an avalanche photodiode (APD, Perkin Elmer SPCM-AQR-14) to record the signal photons transmitted from the Fabry–Pérot, which is tuned by applying a voltage ramp to the piezo-driven mirror mount.

To study correlations between photon pairs, coincidences between signal and idler were characterized by measuring the arrival times of the respective photons with the set-up shown in figure 3. The cross-correlation could be determined measuring coincidences between signal and idler photons by spectrally splitting the photon pair and routing them to separate single-photon detectors (Perkin Elmer single-photon APD for the signal and idQuantique InGaAs APD model id201 for the idler photons). The signal–signal autocorrelation were performed by splitting the signal radiation behind the VBG (i.e., a single cluster was selected) using a 50:50 single-mode fiber coupler (SMFC) and routing the two SMFCs’ output ports to individual silicon APDs. Similarly, there are two InGaAs APDs to catch unfiltered idler photons behind an SMFC.

5. Results and discussion

5.1. PDC clustering and cavity-enhanced spectra

PDC spectra of one waveguide recorded prior and after mirror deposition are shown in figure 4. The spectrum of the uncoated waveguide shows a main peak with a bandwidth (FWHM) of 0.4 nm (≈ 157 GHz), as predicted for the interaction length. The spectra of the same waveguide with dielectric mirrors, however, shows a pronounced sub-structure. Although the resolution of the spectrometer (≈ 0.15 nm) is too coarse to reveal details of the spectra, one can already derive that the pair generation occurs within clusters with a cluster separation of about 0.24 nm (≈ 90 GHz). This separation is determined by the beating of the FSRs of signal and idler, which theoretically are $FSR_s \sim 5.2$ GHz and $FSR_i \sim 5.5$ GHz. Generally, there is one dominant cluster in the center of the normalized phase-matching curve and another two symmetric clusters at the side wings of the envelope, as simulated in figure 1(b).

A comparison of the spectral measurements of the coated and uncoated sample proves already the enhancement of PDC generation in the cavity: If the cavity would only act as a comb filter, only a small fraction of the generated PDC spectrum would ‘transmit’ through this filter. In this case we would have seen only a weak signal for the resonant PDC, because the measured spectra are always convolutions of the real spectra with the spectral resolution, i.e., a window function of about 60 GHz (≈ 0.15 nm) width. In the experiments, however, we observed in both cases spectra with similar intensity levels. For the measurements shown in figure 4(a), all of

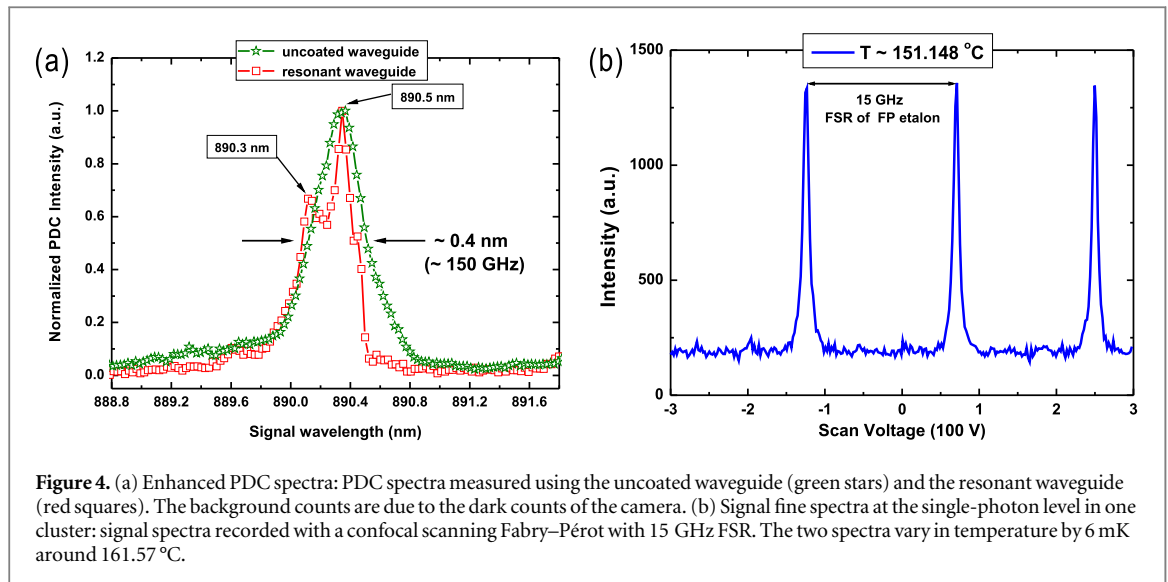


Figure 4. (a) Enhanced PDC spectra: PDC spectra measured using the uncoated waveguide (green stars) and the resonant waveguide (red squares). The background counts are due to the dark counts of the camera. (b) Signal fine spectra at the single-photon level in one cluster: signal spectra recorded with a confocal scanning Fabry–Pérot with 15 GHz FSR. The two spectra vary in temperature by 6 mK around 161.57 °C.

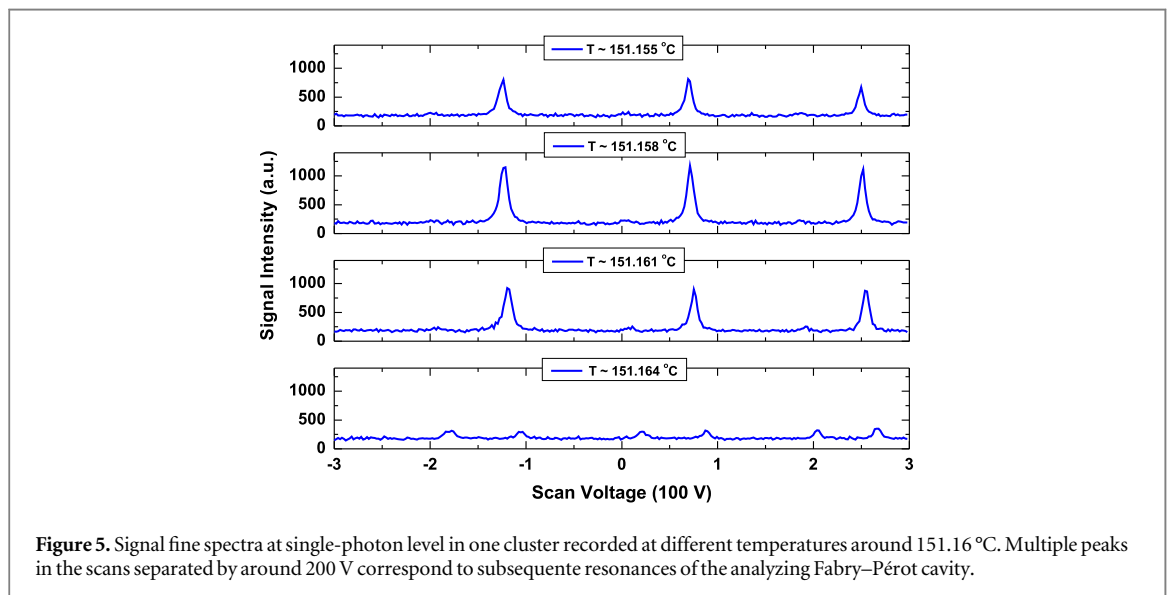


Figure 5. Signal fine spectra at single-photon level in one cluster recorded at different temperatures around 151.16 °C. Multiple peaks in the scans separated by around 200 V correspond to successive resonances of the analyzing Fabry–Pérot cavity.

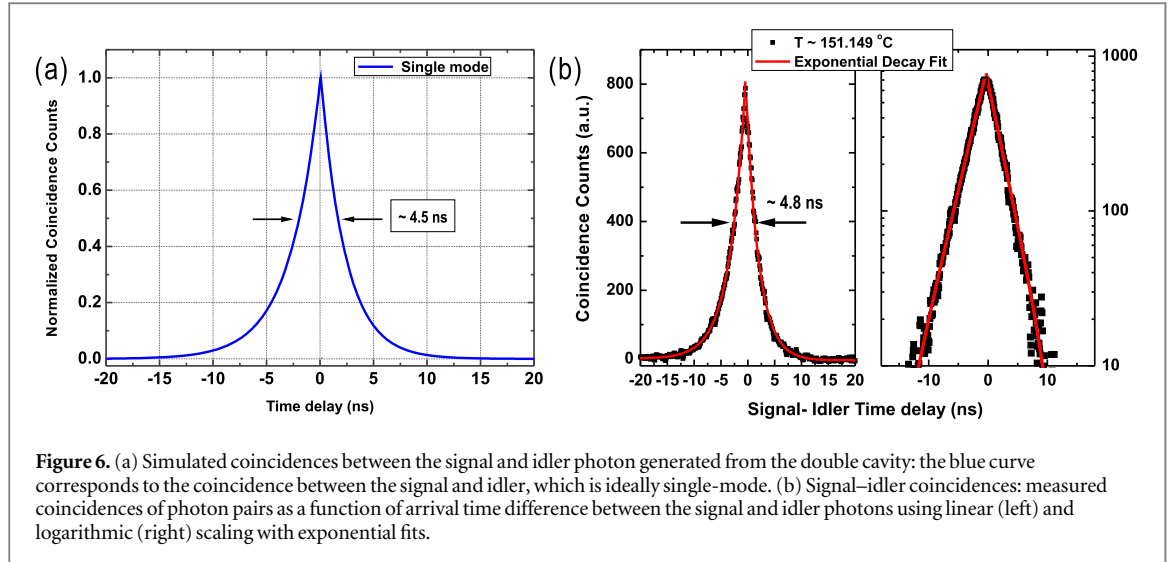
the parameters, apart from adapting the temperature, have been kept constant. In particular, the pump power of about 1 mW in front of the incoupling lens has not been changed. Thus, we can conclude that due to the cavity there is a spectral density redistribution, resulting in an enhanced PDC generation at the resonances.

To study the spectral structure within a single cluster we performed measurements with the scanning Fabry–Pérot resonator. Measured single-photon-level PDC spectra with ~ 700 MHz resolution are shown in figure 4(b). They reveal the modal structure within a single cluster. The spectrum consists of only one longitudinal mode. The scanning range of 15 GHz covers around 3 FSRs of the signal resonator. Please note that the measured linewidth of each longitudinal mode of about 700 MHz is mainly determined by the resolution of the scanning Fabry–Pérot, but it is not the natural bandwidth of the generated PDC photons.

The single-photon level PDC spectra with GHz resolution indicates that we are able to suppress the adjacent ‘satellite’ modes to single-mode operation by finely tuning the temperature—as shown in figure 5. A slight shift of the temperature leads to the spectrum composed of always one predominant mode. Only at a certain temperature does a weak two-mode operation happen.

5.2. Cross-correlation

The temporal second-order signal–idler cross-correlation function [49] is measured as the coincidence counts between the signal and idler photons as function of the arrival time difference (more details were already discussed in 2.4).



To compare the experimental result with the theoretically expected behavior we first simulated the cross-correlation function for the used resonator parameters, assuming a truly single-mode PDC generation, as shown in figure 6(a). The presence of the cavity implies that signal and idler photons may be emitted at distinct times, corresponding to a different number of round trips within the cavity. Thus, the shape of the coincidence curve should be determined by exponential functions. For the multi-mode case the distribution of time of emission differences between the signal and idler modes should show well-defined peaks, with the peak separation corresponding to the cavity round-trip time. However, in our experiment we could not resolve such oscillations due to the finite temporal resolution of our detection system of about 500 ps. The convoluted results concerning the resolution of the detector system is a smooth exponential decay curve as well. Taking into account this limitation again by a convolution of the simulated curves, we find that the bandwidth of the coincidence peak is independent of the number of modes and depends only on the bandwidth of each mode.

In the left diagram of figure 6(b), a result of such a coincidence measurement is shown. It reveals a correlation time (FWHM of the coincidence peak) of about 4.8 ns. This is significantly broader than the corresponding results obtained with non-resonant samples showing a width of about 0.5 ns, which is determined by the finite resolution of our measurement system. The correlation time is inversely proportional to the bandwidth of the down-conversion fields. From the measured correlation time τ_c of 4.8 ns, according to $\tau_c = 1/\pi\Delta\nu$, where $\Delta\nu$ is the bandwidth of the down-converted photons, a spectral bandwidth of about 66 MHz can be deduced. This is in good accordance with the theoretically predicted width calculated for the given cavity parameters, as shown in figure 6(a). In the right diagram of figure 6(b) the measurement result is redrawn, using a logarithmic scaling together with exponential fits for the rising and falling parts. The slight asymmetry reflects the different finesses of signal and idler, resulting in slightly different leakage times out of the resonator. The different slopes of decay lines in logarithmic scaling give us the decay times of the resonators.

Based on the coincidence data and appendix B, the different lifetimes of signal and idler leaving from the resonant waveguide are $\tau_s \sim 3$ ns and $\tau_i \sim 2.4$ ns, respectively. Thus, the loss inside the waveguide cavity can be determined to be as low as $\alpha_s \approx 0.016$ dB/cm and $\alpha_i \approx 0.022$ dB/cm for signal and idler, respectively, as well as cavity finesses of $\mathcal{F}_s \approx 100$ and $\mathcal{F}_i \approx 80$.

5.3. Brightness

The coincidence measurements can also determine the efficiency of the PDC generation process. From the ratio of the coincidence to single counts, the generated photon pair rate can be determined. We found that this rate is almost equal for non-resonant and resonant waveguides. For our source we determined a normalized generation rate (inside the resonator) of about 50×10^6 pairs/(s mW). Assuming these are distributed over three inequivalent clusters with different weights, we can estimate that about 90% of the generated photon pairs are within the most dominant longitudinal mode, with 66 MHz bandwidth. Taking into account the photon-pair escape probability of 5%, the spectral brightness can be estimated to be $B = 3 \times 10^4$ pairs/(s mW MHz).

5.4. Auto-correlation

An alternative method to characterize the spectral properties of the source is the analysis of the auto-correlation Glauber function $g^{(2)}(\tau)$. The number of cavity modes N can be estimated from the measured normalized auto-correlation function at zero time delay, according to $g_m^{(2)}(0) = 1 + 1/N$ (more details are given in appendix C).

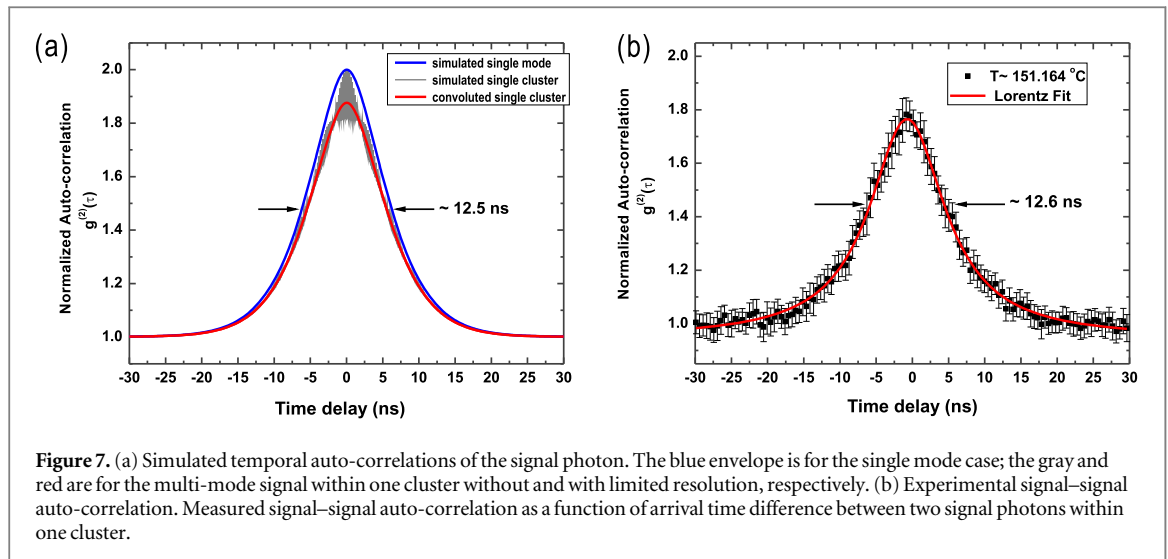


Figure 7(a) provides the simulated and convoluted auto-correlation results for signal photons from the resonant waveguide. In the ideal case of a pure single-cavity mode field, the second-order auto-correlation is close to 2 at zero time delay. For a cluster obtained from this resonant waveguide, which consists of several inequivalent modes (as shown in figures 1(b) and 4(b)), the temporal auto-correlation behavior should reveal multi-mode interference as well. However, we cannot resolve the interference fringes due to the resolution of the detection system. As a result, only one single convoluted peak with lower $g_m^{(2)}(0)$ could be observed in the experiment.

From the measured value $g_m^{(2)}(0) \approx 1.85$, shown in figure 7(b), an effective cavity mode number of $N \approx 1.2$ can be estimated. This is in reasonably good qualitative agreement with the simulated auto-correlation function shown in figure 7(a) and the measured spectra shown in figure 4, where we observed only one mode within a single cluster. The signal auto-correlation time (~ 12.6 ns) is about 2.8 times broader than the signal-idler correlation time (~ 4.8 ns), which is in good agreement with the theoretical analysis (equation (23)). The Lorentz fit to the experimental curve also coincides with our theory model. Moreover, it indicates that shaping single-photon wavepackets by using amplitude and phase modulators is possible [50], because the signal auto-correlation time is much longer than the time jitters from detectors and electro-optic modulators.

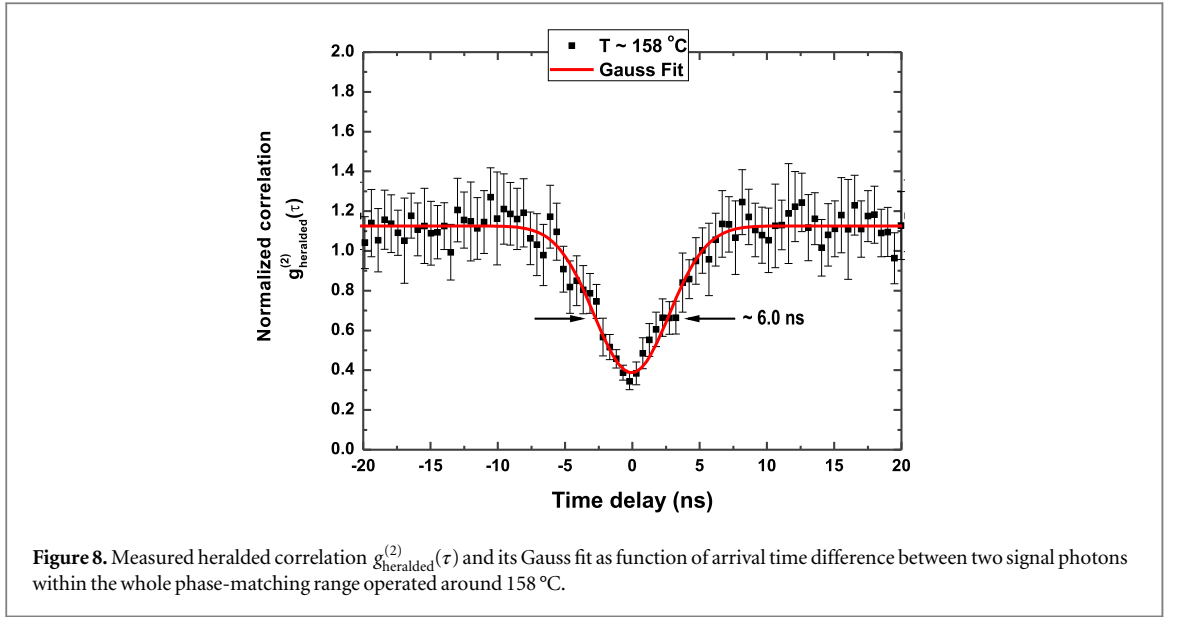
5.5. Heralded correlation

To understand the intrinsic nature of the source, it is important to investigate the heralding performance for this resonant waveguide. The heralding efficiency would suffer from the asymmetric reflectivities, because the photon pairs escaping probability are impacted by the reflectivities of both dielectrics. However, the signal and idler long wave-packets generated from the resonant waveguide could help to resolve the wave-packet of single-signal photons due to the broadened temporal correlation length. The result of the normalized heralded second-order correlation function is shown in figure 8. The $g_{\text{heralded}}^{(2)}(0) < 0.3$ at high pump power (10 mW) confirms a genuine sign of non-classicality. By using low-power pumping (~ 1 mW), the minimum dropped to $g_{\text{heralded}}^{(2)}(0) < 0.02$.

Comparing heralded correlation with auto-correlation, it is found that they have different distributions and bandwidths. The heralded one (~ 6.0 ns) is roughly half of the two-photon auto-correlated one (~ 12.6 ns). The higher-photon components' contributions to heralded correlation measurements mainly influence the minimum value, since the probability to generate single-photon pairs is absolutely higher than the probability to generate double- or even triple-photon pairs.

6. Conclusion

In summary, we have experimentally demonstrated a compact single-longitudinal-mode, two-color narrowband photon-pair source in a doubly resonant Ti:PPLN waveguide. This elaborate source with its compact design demonstrates multiple strengths such as narrow bandwidth, single longitudinal mode, and high brightness, addressing atom and fiber compatibility. Our work shows that clustering can be exploited to restrict PDC generation to a single longitudinal mode. We have also observed several novel experimental phenomena



behind the cavity-enhanced PDC, Cross-correlation time is smaller than auto-correlation time, and two-photon components have longer wave-packets than single ones.

Although the measured bandwidth of about 60 MHz is still about one order of magnitude larger than the smallest bandwidth demonstrated with bulk optical versions [41], our integrated source outperforms the bulk optic realizations in many key features (see also the comparison in table 1). In particular, the rugged design, pure wave-packet, and large brightness of about 3×10^4 pairs/(s mW MHz) are excellent properties of our device, making it a versatile source for various quantum applications, for instance, to address a Nd-based QM with a bandwidth of around 120 MHz [21], a Raman QM with a bandwidth of a few GHz [23], and quantum networks [44]. In general, our source has a great potential for various QCIP applications due to pure state, excellent temporal behavior, and good compatibility with fiber-based systems. Additionally, our device paves the way to arbitrarily shaped single photons in the temporal domain by using integrated devices. Future activities can focus on the development of pure single-mode sources using pulsed light and pulse shaping in a resonant waveguide [43]. Combining clustering with double-pass pumping, to suppress PDC generation to a (filter-free) single-cluster operation [39], and monolithic integration of an electro-optic modulator for fine tuning are further attractive goals.

Acknowledgments

The authors thank Andreas Christ, Regina Kruse, Malte Avenhaus, and Michael Stefszky for useful discussions and helpful comments. This work was supported by the European Union through the QuReP project (no. 247743).

Appendix A. Determining the finesse

In order to ensure that only a single combination of signal and idler modes is in resonance within a cluster, the difference of the FSR for signal and idler must be larger than the spectral width of the single resonances. Assuming that $\text{FSR}_s > \text{FSR}_i$, this leads to the following condition:

$$\text{FSR}_s - \frac{\Delta\nu_s}{2} > \text{FSR}_i + \frac{\Delta\nu_i}{2}, \quad (\text{A.1})$$

where $\Delta\nu_{s,i}$ is the resonance bandwidth for signal and idler, respectively. That is, the difference between different FSRs is required to be larger than the sum of two half-widths from signal and idler. As $\Delta\nu_{s,i} = \text{FSR}_{s,i}/\mathcal{F}_{s,i}$ it follows

$$\left| \text{FSR}_s - \text{FSR}_i \right| > \frac{1}{2} \left| \frac{\text{FSR}_s}{\mathcal{F}_s} + \frac{\text{FSR}_i}{\mathcal{F}_i} \right|. \quad (\text{A.2})$$

From this expression, we can determine the finesse to have only a single mode in the cluster by suppressing adjacent longitudinal modes.

$$\frac{2\mathcal{F}_s\mathcal{F}_i}{n_{gi}\mathcal{F}_i + n_{gs}\mathcal{F}_s} \geq \frac{1}{|n_{gi} - n_{gs}|}. \quad (\text{A.3})$$

If we assume that the cavity has the same finesse for signal and idler, i.e., $\mathcal{F}_s = \mathcal{F}_i = \mathcal{F}$, the finesse is given by

$$\mathcal{F} \geq \frac{1}{2} \left| \frac{n_{gi} + n_{gs}}{n_{gi} - n_{gs}} \right|. \quad (\text{A.4})$$

Appendix B. Photon-pair generation rate and lifetime

In order to design a single-mode source with an integrated waveguide resonator with a precise value of the finesse, one has to optimize the reflectivity of the rear mirror and the length of the waveguide to take into consideration the losses inside the waveguide.

First, let us pay attention to the probability that a photon remains after a round-trip in the resonator, $P_{\text{remain}} = R_1 R_2 e^{-2\alpha L}$, where R_1 and R_2 are the reflectivities of front and rear mirrors, respectively, and α is the internal waveguide loss coefficient. This means the probability that a photon is ‘lost’ in a round trip is given as:

$$P_{\text{lost}} = 1 - R_1 R_2 e^{-2\alpha L}. \quad (\text{B.1})$$

Obviously, the ‘losses’ of such a resonator concept are larger compared to the losses of a single-pass device. Due to multiple round trips in the lossy waveguide, the probability that a photon is lost is increased. As a result, the probability that a photon generated by the PDC process is coupled out of the resonator from the rear mirror R_2 can be estimated as

$$\eta_{s,i} = \frac{1 - R_2}{1 - R_1 R_2 e^{-2\alpha_{s,i} L}}. \quad (\text{B.2})$$

For a pair of photons generated by a PDC process, the photon-pair escape probability η_{pp} , i.e., the probability that a generated pair leaves the resonator at the ‘useful’ port (not necessarily in the same round trip), is given as

$$\eta_{\text{pp}} = \eta_s \eta_i = \frac{1 - R_{2s}}{1 - R_{1s} R_{2s} e^{-2\alpha_s L}} \frac{1 - R_{2i}}{1 - R_{1i} R_{2i} e^{-2\alpha_i L}}. \quad (\text{B.3})$$

Therefore, the efficiency of such resonant photon-pair sources is

$$\eta_{\text{source}} = \eta_{\text{int}} \times \eta_{\text{pp}}, \quad (\text{B.4})$$

where η_{int} is the internal generation efficiency in the waveguide.

Besides the source efficiency, we are also interested in the lifetime $\tau_{s,i}$ of signal/idler photons in the waveguide resonator,

$$\tau_{s,i} = \frac{n_{gs,i} L}{c \ln \left(\sqrt{R_{1s,i} R_{2s,i}} e^{-\alpha_{s,i} L} \right)}. \quad (\text{B.5})$$

Interestingly, the cross-correlation study between signal and idler allows the determination of the cavity performance at signal and idler simultaneously. From the different decay times of the cross-correlation measurements, we can deduce the loss inside the waveguide cavity and the finesse as well at the same time, when the mirror reflectivities are known.

$$\mathcal{F}_{s,i} = \frac{\pi}{1 - e^{-\frac{n_{gs,i} L}{c \tau_{s,i}}}}. \quad (\text{B.6})$$

Appendix C. Multi-mode correlation function

Assume several pairs of signal ω_{sn} and idler modes ω_{in} with narrowband range $\delta\omega$ generated within the broadband phase-matching envelope. Thus, we have a complex JSF

$$f_R(\delta\omega) = \sum_n s_n \frac{\gamma_s}{\gamma_s + i(\delta\omega + \omega_{sn})} \frac{\gamma_i}{\gamma_i - i(\delta\omega - \omega_{in})}, \quad (\text{C.1})$$

where s_n are different phase-matching weights.

In the multi-mode case, the time-dependent signal–idler correlation function can be generalized as

$$G_{si}^{(2)}(\tau) \propto u(\tau) e^{-2\gamma_s \tau} \left| \sum_n s_n e^{-i\omega_{sn} \tau} \right|^2 + u(-\tau) e^{2\gamma_i \tau} \left| \sum_n s_n e^{i\omega_{in} \tau} \right|^2. \quad (\text{C.2})$$

It is found that the coincidence function includes interference terms, resulting in a multi-mode beating under the exponential decay envelope.

If the difference between FSRs is negligible, there are a lot of cavity modes inside one cluster. First, we consider that N signal (idler) resonances occur at distinct central frequencies ω_{sn} (ω_{in}) with equal spacing $\Delta_{FS} = 2\pi\text{FSR}_s$ ($\Delta_{Fi} = 2\pi\text{FSR}_i$). Thus, we rewrite equation (C.2) as

$$G_{si}^{(2)}(\tau) \propto u(\tau) e^{-2\gamma_s \tau} \left[\sum_{n=1}^N s_n^2 + \sum_{n=1}^{N-1} \sum_{j=1}^{N-n} 2s_j s_{j+n} \cos(n\Delta_{FS} \tau) \right] + u(-\tau) e^{2\gamma_i \tau} \left[\sum_{n=1}^N s_n^2 + \sum_{n=1}^{N-1} \sum_{j=1}^{N-n} 2s_j s_{j+n} \cos(n\Delta_{Fi} \tau) \right]. \quad (\text{C.3})$$

This reveals that the two-photon coincidence from a multi-mode cluster is not only determined by two exponential cavity decay times. Additionally, the superposition of different mode beatings contributes from $n\Delta_{FS,j}$. From the above equation, it can be seen that the coincidence distribution consists of two combs of peaks with equal separation, which corresponds to different round-trip times. Then, if the difference between FSRs is large enough, only one mode in each cluster appears. Considering the cluster effect, we rewrite equation (C.2) as

$$G_{si}^{(2)}(\tau) \propto [u(\tau) e^{-2\gamma_s \tau} + u(-\tau) e^{2\gamma_i \tau}] \times \left[C_1 + 2C_2 \cos(2\pi\Delta\nu_{\text{cluster}} \tau) + 2C_3 \cos(4\pi\Delta\nu_{\text{cluster}} \tau) \right], \quad (\text{C.4})$$

where C_i are normalized constants from corresponding phase-matching weights. Both information of cavity mode-beating and cluster modes' interference are included in the two-photon cross-correlation. If we have a stable PDC source with two or three single-mode clusters and a precise detection system, we would also obtain the cluster separation $\Delta\nu_{\text{cluster}}$ from such coincidence measurements.

Generally, for multi-cavity modes and the three-clusters case, the coincidence relationship is more complicated, because mode beating and cluster beating both are involved. If the detection system with perfect resolution could resolve the emission time from different round trips, we could characterize the cavity performance and distinguish the modes' performance, like FSR and cluster separation. However, the description of realistic measurements must take into account the limited temporal resolution of the experimental system. Actually, the time jitter of detector systems at least covers several periods of mode beating and even more periods of cluster beating. Thus, we observed in the coincidence experiment the convolution between the real function and a window function, which is determined by the temporal resolution.

Consider a multi-mode beam with an equally spectral superposition of several Lorentzian distributions,

$$f(\delta\omega) = \sum_n \frac{\gamma_s}{\gamma_s + i(\delta\omega + \omega_{sn})} \frac{\gamma_i}{\gamma_i - i(\delta\omega + \omega_{sn})}. \quad (\text{C.5})$$

The auto-correlation function gives

$$g^{(2)}(\tau) = 1 + \frac{1}{N} |g_0(\tau)|^2 + \frac{1}{N^2} \sum_{n=1}^{N-1} 2(N-n) \cos[n\Delta_F \tau] |g_0(\tau)|^2, \quad (\text{C.6})$$

where Δ_F is the angular FSR and N is the number of modes. When $N = 1$, the third interference term vanishes. In this case, equation (C.6) is the same as equation (22).

For different mode numbers N , we always have $g^{(2)}(0) = 2$, but only for a perfect time resolution. However, realistic detectors suffer from finite time resolution. For our resonant PDC, the photon has longer temporal wave-packets than the time window of the detectors. Therefore, our measurement provides information about the correlation function with finite temporal resolution, which is different from the usual time-integrated measurements, as given, for example, in reference [47]. Assuming that the detection window at zero delay point has a window with width T , then the measured $g_m^{(2)}(0)$ is given by the convolution of the real $g^{(2)}(0)$ with a detector window function. Concerning the realistic measurement, the time window of our detection system is around 0.5 ns, and the Δ_F has a magnitude around tens or hundreds of GHz; i.e., the detector window covers several beating periods. Thus, we observe a time-averaging over the beating periods, resulting in a measured $g_m^{(2)}(0)$ of

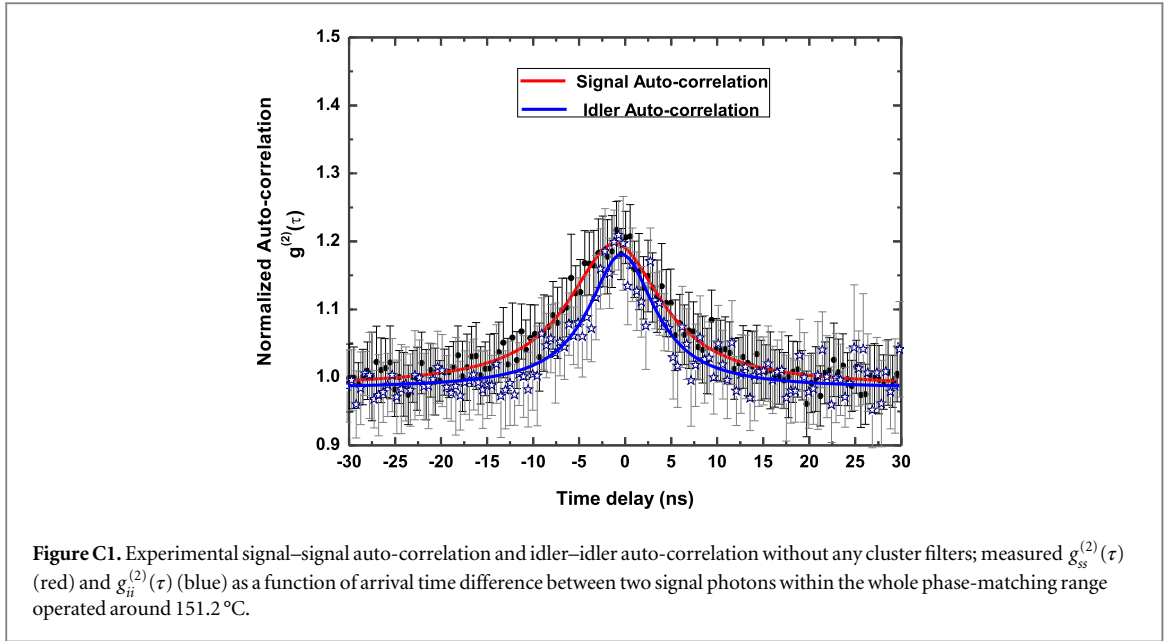


Figure C1. Experimental signal–signal auto-correlation and idler–idler auto-correlation without any cluster filters; measured $g_{ss}^{(2)}(\tau)$ (red) and $g_{ii}^{(2)}(\tau)$ (blue) as a function of arrival time difference between two signal photons within the whole phase-matching range operated around 151.2 °C.

$$\begin{aligned}
 g_m^{(2)}(0) &= 1 + \underbrace{\frac{1}{N} \frac{1}{2T} \int_{-T}^T |g_0(\tau)|^2 d\tau}_{\approx 1} \\
 &+ \underbrace{\frac{1}{N^2} \frac{1}{T} \sum_{n=1}^{N-1} \int_{-T}^T (N-n) \cos[n\Delta_{Fs}\tau] |g_0(\tau)|^2 d\tau}_{\approx 0} \\
 &\approx 1 + \frac{1}{N}.
 \end{aligned} \tag{C.7}$$

Consequently, the number of cavity modes can be directly determined from the auto-correlation measurements. Please note that this conclusion is similar for pulsed time-integrated correlations in reference [47], but cavity modes are not Schmidt modes. As soon as we use a cw laser to pump, we cannot decompose our resonant PDC state to two independent orthonormal bases.

The time-resolved auto-correlation measurement can be used to characterize the spectral longitudinal mode properties of the source. A measured $g_m^{(2)}(0)$ value close to 2 tells that there is only one mode with a thermal photon-number distribution. If more cavity modes are involved, APDs cannot distinguish between the different thermal distributions. The measured value is a convolution between each individual thermal photon stream. It causes the small $g_m^{(2)}(0)$ value in the finite detector window, which tends towards a Poissonian photon-number distribution after detection. If the measurements go further away from the auto-correlation time, the time-averaged correlation function drops to its minimum value one, as expected.

A measured $g_{ss,ii}^{(2)}(\tau)$ characteristic for unfiltered signal and idler beams is shown in figure C1. From the measured value $g_m^{(2)}(0) \approx 1.25$, an effective longitudinal mode number of $N = 4$ can be estimated. This is in reasonably good agreement with the simulated output spectrum shown in figure 1(b), where we estimated one predominantly single mode together with several inequivalent modes within the whole phase-matching envelope. Comparing these two auto-correlation curves, it is found that they have different temporal bandwidths, $T_{au_s} \sim 12.6$ ns and $T_{au_i} \sim 9.7$ ns, respectively, which correspond to the different decay times from the signal and idler cavity. Although signal and idler should have the same bandwidth due to the energy conservation and doubly resonant conditions, the auto-correlation still reveals the different cavity behaviors in the resonant waveguide. The reason is that our pump has a 200 ns pulse length in order to synchronize the generation and detection systems. This means that the pump still has finite bandwidths around 30 MHz in the spectral domain. Besides, the positions of measured $g_{ss,ii}^{(2)}(0)$ slightly shift, just because of imperfect calibrations between two kinds of different detectors (Silicon and InGaAs APDs).

References

- [1] Gisin N, Ribordy G, Tittel W and Zbinden H 2002 Quantum cryptography *Rev. Mod. Phys.* **74** 145–95
- [2] Gisin N and Thew R 2007 Quantum communication *Nat. Photon.* **1** 165–71

- [3] Duan L M, Lukin M D, Cirac J I and Zoller P 2001 Long-distance quantum communication with atomic ensembles and linear optics *Nature* **414** 413–8
- [4] Sangouard N, Simon C, de Riedmatten H and Gisin N 2011 Quantum repeaters based on atomic ensembles and linear optics *Rev. Mod. Phys.* **83** 33–80
- [5] Kimble H J 2008 The quantum internet *Nature* **453** 1023–30
- [6] Politi A, Cryan M J, Rarity J G, Yu S and O'Brien J L 2008 Silica-on-silicon waveguide quantum circuits *Science* **320** 646–9
- [7] Sansoni L, Sciarrino F, Vallone G, Mataloni P, Crespi A, Ramponi R and Osellame R 2010 Polarization entangled state measurement on a chip *Phys. Rev. Lett.* **105** 200503
- [8] Tanzilli S, Martin A, Kaiser F, de Micheli M P, Alibart O and Ostrowsky D B 2012 On the genesis and evolution of integrated quantum optics *Laser Photonics Rev.* **6** 115–43
- [9] O'Brien J, Patton B, Sasaki M and Vučković J 2013 Focus on integrated quantum optics *New J. Phys.* **15** 035016
- [10] Spring J B et al 2013 Boson sampling on a photonic chip *Science* **339** 798–801
- [11] Briegel H J, Dür W, Cirac J I and Zoller P 1998 Quantum repeaters: the role of imperfect local operations in quantum communication *Phys. Rev. Lett.* **81** 5932
- [12] Simon C, de Riedmatten H, Afzelius M, Sangouard N, Zbinden H and Gisin N 2007 Quantum repeaters with photon pair sources and multimode memories *Phys. Rev. Lett.* **98** 190503
- [13] Julsgaard B, Sherson J, Cirac J I, Fiurášcaronek J and Polzik E S 2004 Experimental demonstration of quantum memory for light *Nature* **432** 482–6
- [14] Lvovsky A I, Sanders B C and Tittel W 2009 Optical quantum memory *Nat. Photon.* **3** 706–14
- [15] Reim K F, Nunn J, Lorenz V O, Sussman B J, Lee K C, Langford N K, Jaksch D and Walmsley I A 2010 Towards high-speed optical quantum memories *Nat. Photon.* **4** 218–21
- [16] Hosseini M, Campbell G, Sparkes B M, Lam P K and Buchler B C 2011 Unconditional room-temperature quantum memory *Nat. Phys.* **7** 794–8
- [17] Zhang H et al 2011 Preparation and storage of frequency-uncorrelated entangled photons from cavity-enhanced spontaneous parametric downconversion *Nat. Photon.* **5** 628–32
- [18] Bussi eres F, Sangouard N, Afzelius M, Riedmatten H, Simon C and Tittel W 2013 Prospective applications of optical quantum memories *J. Mod. Opt.* **60** 1519–37
- [19] Afzelius M, Chaneli ere T, Cone R L, Kr oll S, Moiseev S A and Sellars M 2010 Photon-echo quantum memory in solid state systems *Laser Photon. Rev.* **4** 244
- [20] Saglamyurek E, Sinclair N, Jin J, Slater J A, Oblak D, Bussi eres F, George M, Ricken R, Sohler W and Tittel W 2011 Broadband waveguide quantum memory for entangled photons *Nature* **469** 512
- [21] Clausen C, Usmani I, Bussi eres F, Sangouard N, Afzelius M, de Riedmatten H and Gisin N 2011 Quantum storage of photonic entanglement in a crystal *Nature* **469** 508–11
- [22] Riel ander D, Kutluer K, Ledingham P M, Fekete J, Mazzera M and Riedmatten H 2014 Quantum storage of heralded single photons in a praseodymium-doped crystal *Phys. Rev. Lett.* **112** 040504
- [23] Michelberger P S et al 2015 Interfacing GHz-bandwidth heralded single photons with a warm vapour Raman memory *New J. Phys.* **17** 043006
- [24] England D G, Fisher K A G, MacLean J W, Bustard P J, Lausten R, Resch K J and Sussman B J 2015 Storage and retrieval of THz-bandwidth single photons using a room-temperature diamond quantum memory *Phys. Rev. Lett.* **114** 053602
- [25] Burnham D C and Weinberg D L 1970 Observation of simultaneity in parametric production of optical photon pairs *Phys. Rev. Lett.* **25** 84–87
- [26] U'Ren A B, Silberhorn C, Banaszek K and Walmsley I A 2004 Efficient conditional preparation of high-fidelity single photon states for fiber-optic quantum networks *Phys. Rev. Lett.* **93** 093601
- [27] Ou Z Y and Lu Y J 1999 Cavity enhanced spontaneous parametric down-conversion for the prolongation of correlation time between conjugate photons *Phys. Rev. Lett.* **83** 2556–9
- [28] Laurat J, Keller G, Fabre C and Coudreau T 2006 Generation of two-color polarization-entangled optical beams with a self-phase-locked two-crystal optical parametric oscillator *Phys. Rev. A* **73** 012333
- [29] Kuklewicz C E, Wong F N C and Shapiro J H 2006 Time-bin-modulated biphotons from cavity-enhanced down-conversion *Phys. Rev. Lett.* **97** 223601
- [30] Bao X H, Qian Y, Yang J, Zhang H, Chen Z B, Yang T and Pan J W 2008 Generation of narrow-band polarization-entangled photon pairs for atomic quantum memories *Phys. Rev. Lett.* **101** 190501
- [31] Scholz M, Koch L and Benson O 2009 Statistics of narrow-band single photons for quantum memories generated by ultrabright cavity-enhanced parametric down-conversion *Phys. Rev. Lett.* **102** 063603
- [32] Hockel D, Koch L and Benson O 2011 Direct measurement of heralded single-photon statistics from a parametric down-conversion source *Phys. Rev. A* **83** 013802
- [33] Wang F Y, Shi B S and Guo G C 2008 Observation of time correlation function of multimode two-photon pairs on a rubidium D_2 line *Opt. Lett.* **33** 2191–3
- [34] Melholt Nielsen B, Neergaard-Nielsen J S and Polzik E S 2009 Time gating of heralded single photons for atomic memories *Opt. Lett.* **34** 3872
- [35] Wolgramm F, de Icaza Astiz Y A, Beduini F A, Cer e A and Mitchell M W 2011 Atom-resonant heralded single photons by interaction-free measurement *Phys. Rev. Lett.* **106** 053602
- [36] Pomarico E, Sanguinetti B, Gisin N, Thew R, Zbinden H, Schreiber G, Thomas A and Sohler W 2009 Waveguide-based OPO source of entangled photon pairs *New J. Phys.* **11** 113042
- [37] Pomarico E, Sanguinetti B, Osorio C I, Herrmann H and Thew R T 2012 Engineering integrated pure narrow-band photon sources *New J. Phys.* **14** 033008
- [38] Jeronimo-Moreno Y, Rodriguez-Benavides S and U'Ren A B 2010 Theory of cavity-enhanced spontaneous parametric downconversion *Laser Phys.* **20** 1221–33
- [39] Chuu C S, Yin G Y and Harris S E 2012 A miniature ultrabright source of temporally long, narrowband biphotons *Appl. Phys. Lett.* **101** 051108
- [40] F ortsch M, F urst J U, Wittmann C, Strekalov D, Aiello A, Chekhova M V, Silberhorn C, Leuchs G and Marquardt C 2013 A versatile source of single photons for quantum information processing *Nat. Commun.* **4** 1818
- [41] Fekete J, Riel ander D, Cristiani M and de Riedmatten H 2013 Ultranarrow-band photon-pair source compatible with solid state quantum memories and telecommunication networks *Phys. Rev. Lett.* **110** 220502

- [42] Förtsch M *et al* 2015 Highly efficient generation of single-mode photon pairs from a crystalline whispering-gallery-mode resonator source *Phys. Rev. A* **91** 023812
- [43] Kalachev A 2010 Pulse shaping during cavity-enhanced spontaneous parametric down-conversion *Phys. Rev. A* **81** 043809
- [44] Monteiro F, Martin A, Sanguinetti B, Zbinden H and Thew R T 2014 Narrowband photon pair source for quantum networks *Opt. Express* **22** 4371–8
- [45] Eckardt R C, Nabors C D, Kozlovsky W J and Byer R L 1991 Optical parametric oscillator frequency tuning and control *J. Opt. Soc. Am. B* **8** 646–67
- [46] Luo K H, Herrmann H, Krapick S, Ricken R, Quiring V, Suche H, Sohler W and Silberhorn C 2014 An integrated source of high purity single photon pairs with narrow bandwidths *Conf. Lasers Electro-Optics (CLEO) (8–13 June 2014, San Jose CA)* (Piscataway, NJ: IEEE) pp 1–2
- [47] Christ A, Laiho K, Eckstein A, Cassemiro K N and Silberhorn C 2011 Probing multimode squeezing with correlation functions *New J. Phys.* **13** 033027
- [48] Bettelli S 2010 Comment on coherence measures for heralded single-photon sources *Phys. Rev. A* **81** 037801
- [49] Glauber R J 1963 Coherent and incoherent states of the radiation field *Phys. Rev.* **131** 2766–88
- [50] Kolchin P, Belthangady C, Du S, Yin G Y and Harris S E 2008 Electro-optic modulation of single photons *Phys. Rev. Lett.* **101** 103601